

## RESEARCH ARTICLE

# An Adaptive Sliding Mode Control for a Dual Active Bridge Converter With Extended Phase Shift Modulation

FARZANEH BAGHERI<sup>1</sup>, (Member, IEEE), NAKI GULER<sup>2</sup>, (Senior Member, IEEE),  
HASAN KOMURCUGIL<sup>3</sup>, (Senior Member, IEEE), AND  
SERTAC BAYHAN<sup>2,4</sup>, (Senior Member, IEEE)

<sup>1</sup>Department of Electrical and Electronics Engineering, Antalya Bilim University, 07190 Antalya, Turkey

<sup>2</sup>Department of Electrical and Electronic Engineering, Technology Faculty, Gazi University, 06560 Ankara, Turkey

<sup>3</sup>Department of Computer Engineering, Eastern Mediterranean University, 99628 Famagusta, Turkey

<sup>4</sup>Qatar Environment and Energy Research Institute, Hamad Bin Khalifa University, Doha, Qatar

Corresponding author: Sertac Bayhan (sbayhan@hbku.edu.qa)

This work was supported in part by the Scientific and Technology Research Council of Turkey (TUBITAK) under Grant 120E430, in part by the Qatar National Research Fund (a member of Qatar Foundation) under Grant NPRP12S-0214-190083, and in part by the Open Access funding provided by the Qatar National Library.

**ABSTRACT** This paper introduces an adaptive super-twisting sliding mode control (ASTSMC) approach for controlling a dual active bridge (DAB) converter with an extended phase shift (EPS) modulation. The conventional single-phase shift (SPS) modulation-based DAB converter is known to be inefficient. Hence, an optimization algorithm based on the Lagrange multiplier method (LMM) is proposed to minimize both backflow power and inductor current stress simultaneously. Unlike the conventional schemes that use an offline optimization (OFFO) method to derive the phase shift ratios, this paper proposes an online optimization method and an ASTSMC method for generating the inner and outer phase shift ratio respectively. Initially, a generalized average modeling (GAM) for the DAB converter under EPS modulation is derived, and then the proposed ASTSMC is introduced according to this model. The conventional STSMC with constant gains suffers from low performance under disturbances such as load current perturbations, input voltage variations, and output voltage reference variations. Additionally, it requires an overestimated gain under steady-state conditions. To address these issues, a variable gain-based STSMC scheme is proposed to enhance the performance of the converter under all operating conditions. The effectiveness of the proposed method is verified through simulation and experimental results, which are compared with the results of the conventional STSMC method.

**INDEX TERMS** Dual active bridge converter, adaptive super twisting sliding mode control, extended phase shift modulation.

## I. INTRODUCTION

The dual active bridge dc-dc converter has received great attention recently due to its remarkable features such as bidirectional power flow, lower number of passive components, high power density, and high-power efficiency resulting from zero voltage switching (ZVS), high-voltage (HV) conversion ratio and galvanic isolation. Moreover, it is the

The associate editor coordinating the review of this manuscript and approving it for publication was Ahmed Aboushaday<sup>1</sup>.

main device used to interface the battery and supercapacitor as an energy storage device (ESS) to let energy switch between ESSs and the dc microgrid [1], [2], [3]. Various modulation techniques are employed for the DAB converters in literature, which are single phase shift (SPS) [4], extended phase shift (EPS) [5], [6], [7], double phase shift (DPS) [8], [9], [10], and triple phase shift (TPS) [11] modulations. SPS is the conventional modulation scheme which is the simplest one controlling the converter with only one degree of freedom while suffering from inferior

performance at low power regions, limited zero voltage switching (ZVS) zone, high current stress (CS) and high back flow power (BFP) [12]. Compared to the SPS modulation, the EPS modulation provides a wider ZVS zone, less BFP, and lower CS, especially in medium power level. In this power level, although the converter is controlled with the inner phase shift ratio and outer phase shift ratio simultaneously, the inner phase shift ratio is only applied to one of the bridges. Although the DPS employs two control inputs like the EPS, the same inner phase shift ratios should be applied to both bridges. The TPS modulation method has three control inputs which are outer phase shift and two different inner phase shift ratios for the H-bridges. Compared to the TPS and DPS modulation methods, which suffer from the complicated control inputs under different operating conditions and difficulty in implementation, the EPS control with two degree of freedom is simple and easy to analyze and implement while it has reduced control variables and fewer operation modes. In addition, it is useful when only one of the bridges is a fully controlled bridge [13].

Numerous efficiency optimization and dynamic improvement strategies have been investigated in the current state of the art for the DAB converters. These optimization techniques are designed to achieve BFP optimization, CS optimization, and ZVS optimization under various modulation methods. In [5], an optimization method under extended phase shift control is derived to optimize both BFP and CS while the method is an offline calculation technique dependent to the parameters of the system, such as the inductor parameters and not robust enough under perturbations. In [14], [15], and [16], the phase shift ratios are adjusted with an offline technique employing the system parameters. However, the CS and BFP are not optimized simultaneously.

However, the current state of the art tackles this issue by utilizing either an offline optimization-based controller or large data-based methods, both of which are costly and necessitate extensive resources. In [11], [17], [18], and [19] online optimization (ONO) schemes are proposed which aim at improving the efficiency of the DAB. These methods operate on the philosophy of dynamically adjusting the inner phase shift ratios without necessitating power stage calculations.

In [11], an ONO under a unified phase shift (UPS) control is proposed, which is also applicable to other modulation techniques. However, this modulation technique is not efficient in deriving an appropriate model for EPS and does not consider BFP optimization. In [17], a two-dimensional ONO based on a simplex-based optimizer is suggested. A hybrid TPS for optimizing the CS and achieving ZVS in the DAB while adopting the ONO is presented in [18]. In [19], an artificial intelligence-based TPS is adopted to alleviate the challenges of TPS modulation, and the neural network (NN). The authors of [19] utilized a fuzzy inference system (FIS) to attain ONO. However, it is essential to note that all of the above studies use a proportional-integral (PI) controller to regulate the output voltage. Since the DAB converter has

a nonlinear mathematical model, the performance of the PI controller may not be satisfactory. Additionally, the proposed methods are parameter-based. Online optimization modeling free controllers are proposed to simplify the optimization process [19], [20]. In [19], a deep reinforcement learning-based back-stepping control strategy is proposed for a DAB converter connected to constant power loads. This method designs a compensation method based on deep reinforcement learning to intelligently minimize output voltage tracking error and improve the operating efficiency of the system. In [21], a capacitor voltage balancing method is proposed for a neutral-point-clamped based dual-active-bridge converter. To balance the capacitor voltage, a model-free voltage balancing scheme based on a fixed-switching-state method is proposed in this letter. A reactive power minimization and soft switching optimization algorithm for the DAB converter that combines the augmented Lagrangian method (ALM) and triple-phase-shift (TPS) modulation is proposed in [20]. An online minimum reactive power with soft switching algorithm based on the ALM is proposed in this article.

The output voltage of DAB converter may vary due to the changes in load conditions, input voltage, and other factors. Therefore, controlling the output voltage is necessary to maintain the desired power transfer to the load and protect the system from overvoltage or undervoltage conditions. Several methods are developed to control and improve the steady state and dynamic response of the DAB converter, including: feedback control, linearization control, feedforward plus feedback control, disturbance-observer-based control (DOBC), sliding mode control (SMC), and model predictive control (MPC) [22]. The choice of method depends on the specific application requirements, system parameters, and control objectives. A comparison survey among various existing control methods based on their ability to track the output voltage and reject load current perturbations is done in [22]. Reference [23] develops a MPC with current-stress-optimized (CSO) scheme based on dual-phase-shift (DPS) control for a DAB converter in a power electronic traction transformer. Although the proposed method achieves better dynamic performance, but it still suffers of parameter dependency. A non-linear model predictive control (MPC) scheme with phase-shift ratio compensation to improve the dynamic response of the DAB converter is reported in [24]. However, this paper is efficient in controlling the DAB converter with fast time response but it is not applying an optimization method to minimize the losses in the DAB converter. Furthermore, the DAB converter has several challenges that make it difficult to control using conventional control methods. However, the linear PID controllers are well-established method that have been successfully applied in various industrial applications [25], but PID controllers can give a satisfactory control performance only at the operating point, but not under transients [26].

For example, the DAB converter exhibits nonlinear behavior due to the voltage and current stress on the transformer,

and it is also sensitive to variations in the load and input voltage. Therefore, the SMC which is a robust control method is well-suited for controlling the DAB converter due to its advantages over the others including robustness, fast response, implementation simplicity, adaptive capabilities, effectiveness in controlling nonlinear systems, and guaranteed stability of the controlled system even in the presence of disturbances and uncertainties [26], [27], [28], [29], [30], [31].

Nevertheless, the conventional sliding mode control suffers from the chattering phenomenon, which should be suppressed to an acceptable level by using a dedicated technique. The super-twisting sliding mode control (STSMC) method can suppress the chattering with a simple structure and without requiring model parameters [32]. Furthermore, due to its finite time response feature, it can be applied to all systems which have a relative degree of one. However, the STSMC implementation needs information of the gradient of the derivative of the disturbance, which is mostly unknown or overestimated. On the other hand, it is better to adjust the control gain of the STSMC considering the time-varying behavior of the disturbance gradient. The other important point is that the system should operate with a small gain in steady-state while a large gain is needed under disturbances. Therefore, variable gain STSMC is proposed to regulate the control input according to the perturbations of the system [32], [33], [34]. In [32], a STSMC is proposed with variable coefficients, which are functions of the perturbations. The variable gains produced are complicated to calculate and should be applied to the system with bounded perturbations. Since the STSMC includes a sign function with discontinuity under an integral, it can only suppress the chattering without completely removing it. Therefore, the tuning of the control input constants is based on the knowledge of the boundaries of the disturbance gradient, while in many practical cases, this boundary cannot be easily estimated. To overcome this deficiency, the authors in [33] proposed a dynamic variable gain method which is not a function of the bounds of the perturbations but vary dynamically with the variation of the sliding function and its derivative. This method contains a sign function inside the control gains with three different constants that require tuning. In this case, the performance of the STSMC is adversely affected since the DAB is subject to high disturbances of the load current, which can change the operating condition of the system.

This article proposes a simple STSMC for the DAB converter with variable gains which are not dependent to the boundaries of the load current perturbations. Furthermore, on contrary to the method in [35], the control gains are functions of the sliding manifolds rather than the time. The proposed method considers the deviation of the motion around the sliding manifold as a criterion and tunes the gain under a transient perturbation to alleviate the chattering. It is also worth mentioning that the method operates with minimum chattering in the steady state. In addition

to above-mentioned advantages, the control inputs are optimized for the extended phase shift modulation to decrease both current stress and backflow power simultaneously. In summary, the proposed methodology has the following merits.

1) The proposed ASTSMC approach employs an ONO framework with two adjustable degrees of freedom. The outer and inner phase shift ratios serve as the control inputs for the modulation technique. The outer phase shift ratio is an autonomous control variable governed by the ASTSMC algorithm, whereas the inner phase shift ratio is derived by the unique optimization rule calculations deduced by the analytical methods in the paper.

2) The proposed ASTSMC method employs a chattering-free control input with an adaptive variable gain, while the sliding mode-controlled DAB converter in [26] suffers from high chattering and ripples due to the discontinuous control input and the inherent feature of the DAB converter, which is under high disturbances of the load side.

3) On contrary to the recent version of the generalized average modeling (GAM) of the DAB converter, which is constructed based on the SPS method [36], this paper develops the nonlinear GAM of the DAB under EPS method which is a function of the inner and outer phase shift control ratios.

4) On contrary to the literature [6], which needs the output power to estimate the inner phase shift ratio according to the transmitted power under each operating point, in the proposed method, the inner phase shift ratio is a function of the outer phase shift ratio and adaptable to the operating point variations automatically and doesn't need to measure the output current.

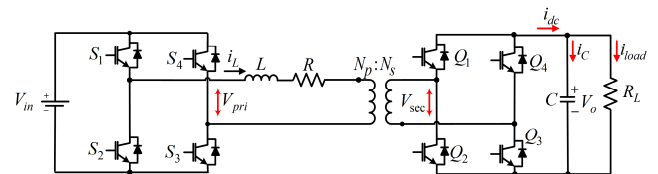
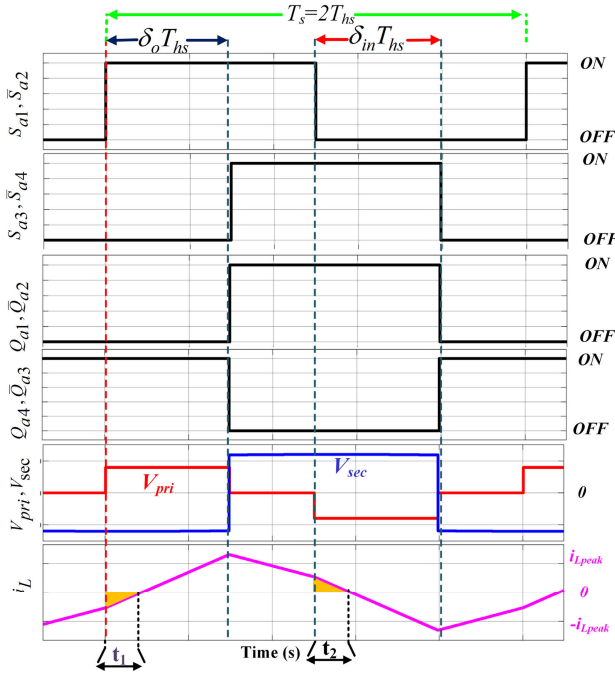


FIGURE 1. Bidirectional dual active bridge converter.

## II. ANALYSIS OF EPS MODULATION FOR DAB

Fig. 1 depicts the main topology of a single-phase DAB converter feeding a resistive load ( $R_L$ ). It comprises of two full bridges that are isolated by a high-frequency transformer. The DAB converter comprises three stages. The first stage is a full bridge inverter which converts the input DC voltage ( $V_{in}$ ) to AC voltage ( $V_{pri}$ ). In the second stage, a high-frequency transformer steps up (or down)  $V_{pri}$  or offers galvanic isolation only when the turn ratio is equal to one. In the final stage, a full bridge rectifier converts the AC voltage ( $V_{sec}$ ) to a DC voltage ( $V_o$ ) which may feed a load or a battery. In this topology,  $V_{in}$  and  $V_o$  are the dc-link voltages,  $L$  is the lumped leakage inductance of the primary and secondary side of the transformer and  $R$  is the internal loss of the inductance.

Since the inductance value is selected based on the power reference, the value of  $L$  can be tuned by adding an external inductance to the system. The semiconductor switches in the primary and secondary sides are denoted by  $S_1 - S_4$  and  $Q_1 - Q_4$ , respectively. The gate pulses applied to the switches are labeled as  $S_{a1} - S_{a4}$  and  $Q_{a1} - Q_{a4}$ .



**FIGURE 2.** Standard waveforms of the gate signals,  $V_{pri}$ ,  $V_{sec}$  and  $i_L$  with EPS modulation.

In the EPS modulation method,  $V_{pri}$  is a 3-level voltage rather than a square wave. Thus, another phase shift is introduced between  $S_1 - S_4$ . The typical waveforms of the DAB converter, which are the gate signals applied to the switches,  $V_{pri}$ ,  $V_{sec}$  and  $i_L$  under EPS modulation, are given in Fig. 2. While the inner phase shift ratio between  $S_1 - S_4$  is denoted by  $\delta_{in}$ , the outer phase shift ratio between the primary and secondary bridge is represented by  $\delta_o$ . The transmitted power can be regulated if  $\delta_o$  is employed as the control input, while  $\delta_{in}$  can be tuned to mitigate the large amount of BFP and high CS. The switching time and half of the switching time are denoted by  $T_s$  and  $T_{hs}$ , respectively. If  $k = V_{in}/NV_o$  and  $N = N_p/N_s$ , then  $k < 1$  means boost operation. In Fig. 2, while the gate signal  $S_{a1}$  lags  $S_{a4}$  causing a 3-level voltage at the primary bridge terminals, the gate signal  $S_{a1}$  leads  $Q_{a1}$  to transmit power from the primary side to the secondary side of the converter. While  $i_L$  is represented for one switching period, the BFP areas which are adverse transfer of power are highlighted with dark yellow in Fig. 2. In these intervals which are denoted by  $t_1$  and  $t_2$ , the polarities of  $V_{pri}$  and  $i_L$  are opposite. It is worth remarking that the BFP can be decreased considerably by tuning  $\delta_{in}$ .

The normalized transmitted power ( $P_T$ ), normalized back-flow power ( $P_B$ ) and normalized maximum current of the

inductor ( $I_p$ ) under EPS method are written as follows [5]:

$$P_T = 4\delta_o(1 - \delta_o) + 2\delta_{in}(1 - \delta_{in} - 2\delta_o) \quad (1)$$

$$P_B = \begin{cases} \frac{[k(1-\delta_{in})+(2\delta_o-1)]^2}{2(k+1)}k \geq 1 \\ \frac{[M(1-\delta_{in})+(2\delta_o-1)]^2}{2(M+1)}k < 1 \end{cases} \quad (2)$$

$$I_p = \begin{cases} 2[k(1 - \delta_{in}) + (2\delta_o + 2\delta_{in} - 1)]k \geq 1 \\ 2[(1 - \delta_{in}) + k(2\delta_o + 2\delta_{in} - 1)]k < 1 \end{cases} \quad (3)$$

where  $M = 1/k$ . The normalized powers ( $P_T$  and  $P_B$ ) are the fraction of the maximum power ( $P_{max} = \frac{NV_{in}V_o}{8Lf_s}$ ) and the normalized current stress ( $I_p$ ) is the fraction of the maximum current stress ( $I_{max} = \frac{NV_o}{8Lf_s}$ ) where  $f_s$  is the switching frequency. Since half of the switching time ( $T_{hs}$ ) has symmetry to the other half, all equations mentioned above are derived for the half switching time  $T_{hs}$ .

To regulate  $\delta_{in}$ , an optimization algorithm should be applied to  $i_L$  and BFP under EPS modulation control. For a normalized transmitted power reference ( $P_T^*$ ), one can minimize BFP and current stress ( $I_p$ ) for a specific amount of  $\delta_{in}$ . Thus, two Lagrange functions can be identified as follows

$$G_1(\delta_o, \delta_{in}, \lambda_1) = P_B + \lambda_1(P_T - P_T^*) \quad (4)$$

$$G_2(\delta_o, \delta_{in}, \lambda_2) = I_p + \lambda_2(P_T - P_T^*) \quad (5)$$

where  $\lambda_1$  and  $\lambda_2$  are the Lagrange multipliers.

The relationship between  $\delta_o$  and  $\delta_{in}$  can be obtained based on the principle of the Karush–Kuhn–Tucker (KKT) conditions [35]. The Lagrange functions in (4) and (5) can be solved by the primal feasibility as follows

$$\nabla G_1(\delta_o, \delta_{in}, \lambda_1) = 0 \quad (6)$$

$$\nabla G_2(\delta_o, \delta_{in}, \lambda_2) = 0 \quad (7)$$

It should be noticed that the system of equations (6)-(7) have four equations which can be expanded as follows

$$\langle P_{B\delta_o} \ P_{B\delta_{in}} \rangle + \langle \lambda_1 P_{T\delta_o} \ \lambda_1 P_{T\delta_{in}} \rangle = 0 \quad (8)$$

$$\langle I_{p\delta_o} \ I_{p\delta_{in}} \rangle + \langle \lambda_2 P_{T\delta_o} \ \lambda_2 P_{T\delta_{in}} \rangle = 0 \quad (9)$$

$$P_T^* + 4\delta_o^2 - 4\delta_o + 2\delta_{in}^2 - 2\delta_{in} + 4\delta_{in}\delta_o = 0 \quad (10)$$

where  $\langle \rangle$  denotes the expansion of the gradient vectors in (6) and (7). Solving (8)-(10) concurrently for  $k \geq 1$  yields  $\delta_o$  and  $\delta_{in}$  in terms of  $P_T^*$  as follows

$$\delta_o = \begin{cases} \frac{f(z_1) - \sqrt{f(z_1)(1-P_T^*)}}{2f(z_1)} BFP \ P_T^* \geq \frac{2(k+1)}{(k+2)^2} \\ \frac{f(g_1) - \sqrt{f(g_1)(1-P_T^*)}}{2f(g_1)} CS \ P_T^* \geq \frac{2(k-1)}{(k)^2} \end{cases} \quad (11)$$

$$\delta_{in} = \begin{cases} z_1(1 - \frac{f(z_1) - \sqrt{f(z_1)(1-P_T^*)}}{f(z_1)}) BFP \\ g_1(1 - \frac{f(g_1) - \sqrt{f(g_1)(1-P_T^*)}}{f(g_1)}) CS \end{cases} \quad (12)$$

where  $z_1 = \frac{(k+1)}{(k+2)}$ ,  $g_1 = \frac{(k-1)}{k}$ ,  $f(z_1) = (2z_1^2 - 2z_1 + 1)$  and  $f(g_1) = (2g_1^2 - 2g_1 + 1)$ . Fig. 3 shows the range of variation of  $\delta_o$  and  $\delta_{in}$  according to (11)-(12) alongside  $P_T^*$  versus  $k$  for both BFP and CS optimizations. The variation of  $\delta_o$  and  $\delta_{in}$  under different  $P_T^*$  are visible, while the solid line is the CS optimization result, and the dashed line depicts the



BFP optimization result. Considering Fig. 3(a), one can see that the outer phase shift ratio monotonically increases while the power is increased for both CS and BFP optimization. Moreover, observing the variation of both phase shifts versus the variations of  $k$ , one can see that the  $\delta_o$  and  $\delta_{in}$  curves reach to a steady state region for large  $k$  values.

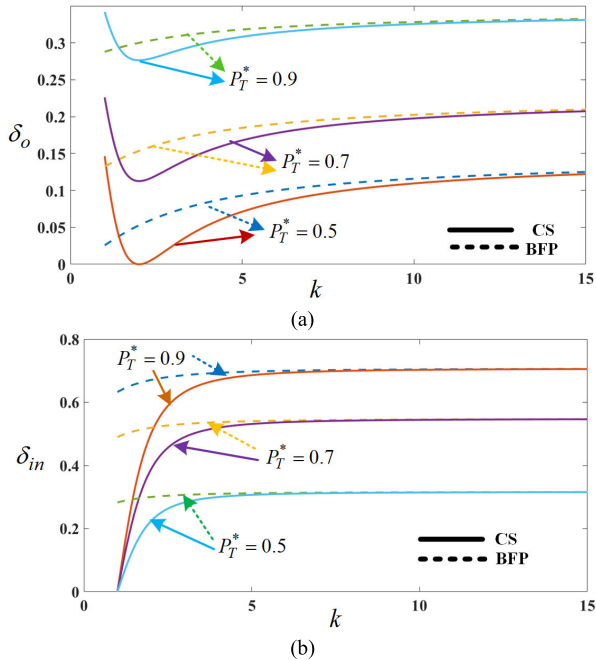


FIGURE 3. The variation of  $\delta_o$  and  $\delta_{in}$  alongside variation of  $P_T^*$  and  $k$  when  $k \geq 1$ . (a)  $\delta_o$  versus  $k$ , (b)  $\delta_{in}$  versus  $k$ .

Fig. 3(b) shows the variation of  $\delta_{in}$  when  $P_T^*$  and  $k$  are changed. Obviously, both CS and BFP cannot be optimized simultaneously for  $k \leq 2$ . When  $k \leq 2$ , the minimization of both CS and BFP does not occur at the same inner phase shift ratio. Consequently, it is impossible to optimize both CS and BFP using the same inner phase shift ratio, as they are achieved at different values. For instance: If  $k = 1.5$  and  $P_T^* = 0.7$ , the purple solid line and the yellow dashed line are showing the CS and BFP optimization curves respectively. Hence, the inner phase shift ratio ( $\delta_{in}$ ) can be deduced from these curves as

$$\delta_{in} = 0.5106 \text{ for minimization of BFP}$$

$$\delta_{in} = 0.2420 \text{ for minimization of CS}$$

As a result, it is not feasible to achieve the minimization of both objectives using a single parameter. Hence, when  $1 < k < 2$ , the proposed approach is recommended solely for the minimization of BFP, while the SPS method is suggested for the minimization of CS. When  $k \geq 2$ , the optimized regions of CS and BFP occur around the same points.

For analyzing the case  $k < 1$ , similar equations to (11)-(12) can be derived whereas  $z_1$  is replaced by  $z_2 = \frac{(k+1)}{(2k+1)}$  and  $g_1$  is replaced by  $g_2 = 1/(k+1)$ .

Fig. 4 illustrates the variation of the phase shift ratios along with the variations of the unified power reference for  $k < 1$ . Inspecting Fig. 4(b), one can see that both CS and BFP

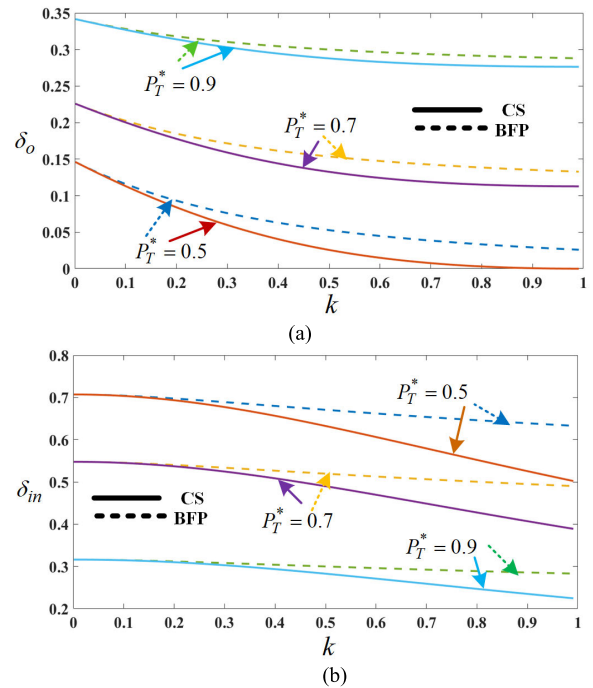


FIGURE 4. The gradual variation of  $\delta_o$  and  $\delta_{in}$  alongside variation of  $P_T^*$  when  $k < 1$ . (a)  $\delta_o$  versus  $k$ , (b)  $\delta_{in}$  versus  $k$ .

minimization occurs concurrently for  $0 \leq k \leq 0.3$ . However, when  $k$  is increased, the optimization regions are different. The concurrent optimization cannot occur around  $k = 1$ , and one of the targets should be selected or SPS modulation can be applied to minimize the current stress.

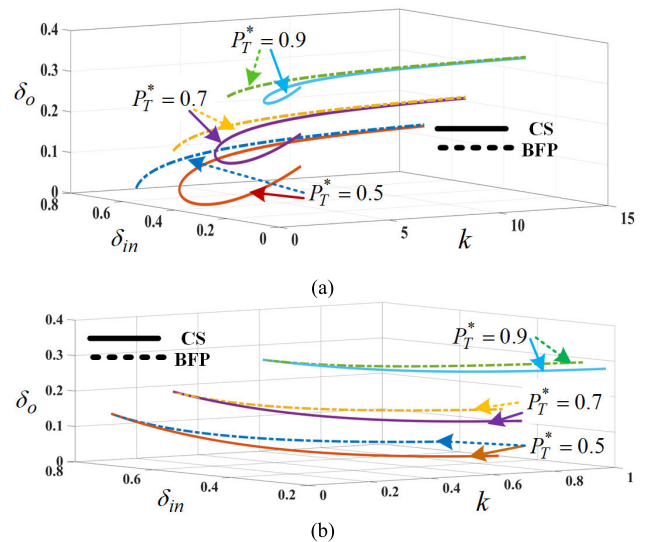


FIGURE 5. The variation of  $\delta_o$  and  $\delta_{in}$  alongside variation of  $P_T^*$  and  $k$  when (a)  $k \geq 1$ , (b)  $k < 1$ .

Fig. 5 depicts the three-dimensional variation of  $\delta_o$ ,  $\delta_{in}$  and  $k$  alongside changes of  $P_T^*$ . Fig 5(a) shows the optimized operating points for  $k \geq 1$  and Fig 5(b) depicts the optimized operating points for  $k < 1$ . Thus, when  $k \leq 2$ , the CS is minimized if the DAB converter works under SPS modulation

which means that  $\delta_{in} = 0$ , whereas BFP minimization occurs at a different  $\delta_{in}$ . Therefore, for some boundaries of  $k$ , both CS and BFP cannot occur at the same time and the optimization can be applied either optimizing BFP or CS. To find an ONO, the relationship between the output value of the control and the phase shift ratios should be discussed. Therefore, a rule can be achieved to regulate both phase shifts simultaneously. Since  $\delta_o$  has a proportional relation to the unified power, the control method output can be applied to the system as the outer phase shift ratio. On the other hand,  $\delta_{in}$  has also the relation according to (12) with the unified power which can be applied to the system as  $\delta_{in}$ .

The monotonic increment of  $\delta_o$  versus the transmitted power is clear in both figures. As a result,  $\delta_o$  can be considered as the independent control input to the system from the ASTSMC strategy. On the other hand, under large  $k$  values in Fig. 5(a) and for  $0 \leq k \leq 0.3$  in Fig. 5(b), both BFP and CS can appear concurrently. Therefore, according to the results obtained from (11) and (12) and the explanations given for Fig. 3 and Fig. 4, the following ONO rule can be applied to the DAB converter to acquire  $\delta_{in}$ :

$$\delta_{in} = \begin{cases} 1 - \left(\frac{k+1}{2k+1}\right)\delta_o & 0 < k < 0.3 \\ \begin{cases} 1 - \left(\frac{k+1}{2k+1}\right)\delta_o & \text{less BFP} \\ \text{SPS} & \text{less CS} \end{cases} & 0.3 \leq k < 1 \\ \begin{cases} 1 - \left(\frac{k+1}{k+2}\right)\delta_o & \text{less BFP} \\ \text{SPS} & \text{less CS} \end{cases} & 1 < k \leq 2 \\ 1 - \left(\frac{k-1}{k}\right)\delta_o & k > 2 \\ \text{SPS} & k = 1 \end{cases} \quad (13)$$

Fig. 6 displays the normalized current stress and backflow power based on the online verification of the proposed strategy given in equation (13). The solid lines show the proposed EPS method results and the plus marked lines show the SPS method results. Focusing on this figure, one can see that the figure compares the EPS and SPS results for 3 different  $k$  values. The outer phase shift ratio has the same variation for both methods. According to Fig. 6(a) for  $0 < k < 0.3$ , the proposed EPS method is paramount in both BFP and CS reduction. However, while  $0.3 \leq k < 1$ , the proposed method is superior compared to SPS in BFP reduction whereas SPS is superior in CS reduction.

Fig. 6(b) elaborates same comparison while  $k > 1$ . The CS and BFP are calculated and shown for the proposed EPS and SPS methods. Considering this figure, one can see that while  $1 < k \leq 2$ , less BFP is generated with the proposed method while less CS can be attained with SPS method. For  $k > 2$ , the proposed method can be applied to the system for both BFP and CS reduction simultaneously since it outperforms the SPS method.

### III. MATHEMATICAL MODELING OF THE DAB CONVERTER UNDER EPS MODULATION

The mathematical modeling of the DAB converter in this paper is based on the generalized average modeling (GAM)

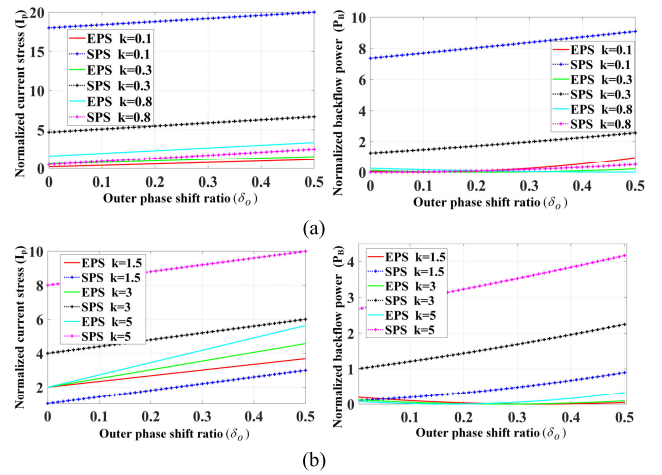


FIGURE 6. Normalized current stress and backflow power under EPS and SPS methods. (a)  $k < 1$ , (b)  $k > 1$ .

which is dedicated based on the Fourier series of the pulses applied to the switches of the bridges [37]. Since this paper intends to derive the dynamics of  $i_L$  and  $V_o$  as a function of  $\delta_{in}$  and  $\delta_o$ , the GAM explored in the state of the art is modified in this article. To derive the state space model of the DAB converter, the Fourier series of all the pulses of the switches are derived as the function of  $\delta_{in}$  and  $\delta_o$  as follows:

$$S_{am} = Q_{am} = \frac{1}{2} + \frac{2}{\pi} \sum_{n=odd} \frac{\sin(2n\pi f_s t - n\theta)}{n} \quad (14)$$

where  $S_{am}$  and  $Q_{am}$  are the pulses applied to the switches  $S$  and  $Q$ ,  $\theta$  depicts the inner or outer phase shift angle between the switches of the primary bridge or the switches of the primary and the secondary bridge and  $n$  is the order of the odd harmonics. The primary and secondary voltages of the transformer can be derived as

$$V_{pri} = V_{in}(S_{a1}(t) - S_{a4}(t)) \quad (15)$$

$$V_{sec} = V_o(Q_{a1}(t) - Q_{a4}(t)) \quad (16)$$

The capacitor current can be calculated as

$$i_C = i_{dc} - i_{load} = i_L(Q_{a1}(t) - Q_{a4}(t)) - i_{load} \quad (17)$$

If  $S_{a1}$ ,  $S_{a4}$ ,  $Q_{a1}$  and  $Q_{a4}$  are calculated from (14) and replaced in (17), then the final nonlinear differential equation of the output voltage of the DAB converter can be derived as

$$\begin{aligned} \frac{dV_o}{dt} &= \frac{i_C}{C} \\ &= \frac{16NV_{in}}{C\pi^2} \sum_n \frac{1}{2n^2 |Z_n|} \cos\left(\frac{n\delta_{in}}{2}\right) \cos\left(\frac{n\delta_{in}}{2} - \theta_n + n\delta\right) \\ &\quad - \frac{16N^2V_o}{C\pi^2} \sum_n \frac{1}{2n^2 |Z_n|} \cos(\theta_n) - \frac{i_{load}}{C} \end{aligned} \quad (18)$$

where  $n = 1, 3, 5, \dots$  depicts the order of the harmonics and

$$|Z_n| = \sqrt{R^2 + (2nL\pi f_s)^2}, \theta_n = \tan^{-1}\left(\frac{2nL\pi f_s}{R}\right) \quad (19)$$

Since this paper aims to develop an ASTSMC (see section IV) which is robust enough to attenuate the effect of uncertainty and the disturbances, on the contrary to the state of the art, it is not required to linearize (18) around an operating point. Therefore, after considering  $n = 1$ , (18) can be rewritten as

$$\frac{dV_o}{dt} = A\gamma(u) - F - BV_o \quad (20)$$

where

$$\gamma(u) = \cos\left(\frac{\delta_{in}}{2}\right) \cos\left(\frac{\delta_{in}}{2} - \theta_1 + \delta_o\right) \quad (21)$$

$$A = \frac{8V_{in}N}{C|Z_1|\pi^2}, B = \frac{8N^2}{C|Z_1|\pi^2} \cos(\theta_1), u = [\delta_o \delta_{in}] \quad (22)$$

where  $\gamma(u)$  is the nonlinear control input and  $F$  is the disturbance given by

$$F = i_{load}/C \quad (23)$$

Since normally the internal resistance ( $R$ ) of the inductance is very small compared to the inductive reactance ( $X_L$ ), so considering  $\theta_1 = 90^\circ$  in (21) yields:

$$\gamma(u) = 0.5[\sin(\delta_{in} + \delta_o) + \sin(\delta_o)] \quad (24)$$

Consequently, the generalized average model of the DAB converter is obtained.

#### IV. ADAPTIVE STSMC METHOD

SMC is a powerful control technique that is widely used for controlling various dynamic systems. Its goal is to create a sliding motion in the system's state space and drive the system's state trajectory onto a predefined sliding surface, which is designed to ensure a desired system behavior. In order to achieve the sliding motion, a control law that generates a switching signal forcing the system's state trajectory to converge onto the sliding surface should be designed. The sliding surface is a mathematical concept that is defined in the state space of the system, and it is designed to ensure a desired behavior for the system. In this study, the super twisting control law is chosen to reach and slide on the surface.

The sliding surface for controlling the output voltage of the DAB converter is considered as follows:

$$\sigma = (V_o - V_o^*) \quad (25)$$

where  $V_o^*$  is the reference output voltage. Taking derivative of (25) and substituting (20) into the resulting equation yields

$$\dot{\sigma} = d(t) + A\gamma(u) \quad (26)$$

where  $d(t)$  is defined as

$$d(t) = -B\sigma - BV_o^* - F \quad (27)$$

Suppose that  $d_o = d(t)/A$  satisfies the following inequality for some unknown positive constant  $\eta$

$$|\dot{d}_o| \leq \eta |\sigma|^{1/2} \text{sign}(\sigma) \quad (28)$$

If a proper Lyapunov function is selected [38], [39], one can prove that the sliding trajectory and its derivative reach the equilibrium point in finite time and slide along the manifold under the STSMC control law given in (29).

$$\begin{cases} \dot{\delta}_o = -k_1 |\sigma|^{1/2} \text{sign}(\sigma) + v \\ \dot{v} = -k_2 \text{sign}(\sigma) \end{cases} \quad (29)$$

where  $k_1$  and  $k_2$  are the control gains. Considering that  $\varphi = v + d_o$ , then, to attain the dynamics of the system under STSM, equation (29) is substituted in (24) which yields

$$\begin{cases} \dot{\sigma} = A(-k_1 |\sigma|^{1/2} \text{sign}(\sigma) + \varphi) \\ \dot{\varphi} = -k_2 \text{sign}(\sigma) + \dot{d}_o \end{cases} \quad (30)$$

The closed loop STSMC gets the feedback of the output voltage and then constructs the sliding surface ( $\sigma$ ) according to (29) and then calculated the control law which requires the sliding surface as the input and tuning two parameters ( $k_1$  and  $k_2$ ). Compared with the traditional second order sliding mode control, the STSMC only needs the information of the sliding surface. However, it suffers from the complexity in tuning the control gains ( $k_1$  and  $k_2$ ). Thus, in practice overestimating these gains, not only leads to larger than necessary gains, but also requires the information of the limit of the disturbance ( $\eta$ ). Since determining  $\eta$  is difficult, so the adaptive super twisting sliding mode control (ASTSM) algorithm has strong engineering significance to estimate the gains  $k_1$  and  $k_2$ . The adaptive gains should be defined in such a way that  $\sigma$  and  $\dot{\sigma}$  are derived to zero in finite time in the presence of the bounded disturbance. For any initial conditions, the super twisting control input (29) can enforce the sliding manifold and its derivative to zero under the following adaptive sliding coefficients:

$$k_1(\sigma) = \begin{cases} \frac{l_o}{\sqrt{\varepsilon - |\sigma|}}, & |\sigma| < \varepsilon \\ l_1(1 - e^{-\lambda|\sigma|}), & |\sigma| > \varepsilon \end{cases} \quad (31.a)$$

$$(31.b)$$

$$k_2(\sigma) = 2\beta k_1 \quad (32)$$

where  $l_o$ ,  $l_1$ ,  $\lambda$  and  $\beta$  are the adaptation positive constants and  $\varepsilon$  is a very small chattering value that can exist over the sliding manifold ( $\sigma$ ) in the steady state. To prove that the proposed method achieves finite time response, the following steps are considered.

Let us assume that initially, the sliding manifold magnitude ( $|\sigma|$ ) is much more than the defined error ( $\varepsilon$ ). So, equation (31.b) is triggered enhancing the variable gain as far as  $|\sigma| < \varepsilon$ . Then (31.a), which is a barrier function starts functioning and the variable gain is still a function of sliding manifold and error. Initially, it should be proved that there is a finite time for which the sliding manifold ( $\sigma$ ) given in (25) will reach the boundary  $|\sigma| < \varepsilon$  under the variable gain (31.a)-(32). To prove it, first assume that  $|\sigma| > \varepsilon$ , thus, from (31.a) one can derive the variable gain as  $l_1(1 - e^{-\lambda|\sigma|})$  which is an increasing exponential function and has a maximum of  $l_1$  growing with the slope of  $\lambda$ . The system tracks the corresponding trajectory as long as  $|\sigma| > \varepsilon$ . Let the interval of this trajectory being considered as  $I(\sigma)$ . Then, if one proves

that the period of  $I(\sigma)$  is finite, then the finite time response is satisfied. During this interval, the following inequalities can be deduced from (30):

$$\begin{aligned} -k_2 - \eta < \dot{\varphi} < -k_2 + \eta \\ -2\beta l_1(1 - e^{-\lambda|\varepsilon|}) - \eta < \dot{\varphi} < -2\beta l_1 + \eta \end{aligned} \quad (33)$$

In this interval,  $\varphi(t)$  becomes zero and remains negative. The first equation of (30) is then rewritten as  $\dot{\sigma} \leq -Ak_1 |\sigma|^{1/2} \text{sign}(\sigma)$  and, hence,  $\sigma$  converges to zero in finite time.

To prove the stability of the proposed method, a Lyapunov analysis is required. The Lyapunov analysis is a powerful mathematical tool for proving stability of nonlinear systems. To perform the stability using Lyapunov analysis in sliding mode control, a Lyapunov function is first defined. Now, consider a new state vector which is introduced as

$$z^T = [z_1 z_2] = [|\sigma|^{1/2} \text{sign}(\sigma) \varphi] \quad (34)$$

The derivative of the new state variable ( $z$ ) can be derived as

$$\dot{z}^T = \left[ \frac{1}{2|z_1|} \dot{\sigma} \dot{\varphi} \right] \quad (35)$$

Let us replace (30) in (35) which yields

$$\dot{z} = \bar{A}z = \frac{1}{2|z_1|} \begin{bmatrix} -Ak_1 & A \\ -4\beta k_1 + \eta & 0 \end{bmatrix} z \quad (36)$$

The following quadratic Lyapunov function [40], is designed to investigate the stability analysis of the proposed method

$$V(z) = z^T p z \quad (37)$$

where  $p$  is a symmetric positive definite matrix with  $\varepsilon_1$  and  $\beta$  the real positive numbers as defined below

$$p = \begin{bmatrix} 4\beta + \varepsilon_1^2 & -\varepsilon_1 \\ -\varepsilon_1 & 2 \end{bmatrix} = p^T > 0 \quad (38)$$

Thus,  $V(z)$  is positive definite function and its time derivative along the solution of the system can be derived as

$$\dot{V}(z) = \dot{z}^T p z + z^T p \dot{z} \quad (39)$$

Substituting (36) in (39) yields

$$\dot{V}(z) = z^T (\bar{A}^T p + p \bar{A}) z \leq -\frac{1}{2|z_1|} z^T Q z \quad (40)$$

Using the bounds on the perturbation (28), it can be shown that

$$Q \leq \begin{bmatrix} 8Ak_1\beta & A(\varepsilon_1 k_1 - 4\beta - \varepsilon_1^2) \\ A(\varepsilon_1 k_1 - 4\beta - \varepsilon_1^2) & 2A\varepsilon_1 \end{bmatrix} \quad (41)$$

So,  $\dot{V}(z)$  is negative definite if  $Q$  is a positive definite matrix which can be guaranteed if  $k_1$  is selected as

$$k_1 = \frac{\eta}{(-\varepsilon_1 A + 4\beta)} \quad (42)$$

$$0 < 2k_1 < (16\beta - 1) + \sqrt{5 + 320\beta^2} \quad (43)$$

Therefore, considering the developed boundaries,  $\sigma$  converges to zero in finite time and remains inside the definite bandwidth ( $\varepsilon$ ) despite the perturbations.

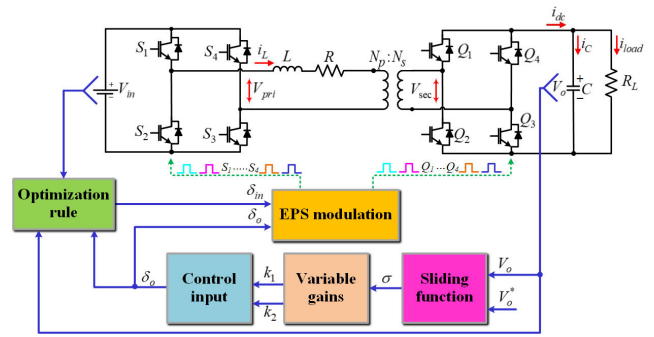


FIGURE 7. Control diagram of the proposed method for the DAB converter.

## V. SIMULATION AND EXPERIMENTAL RESULTS

The performance of the DAB converter with the proposed optimized ASTSMC method is investigated through simulation and experimental studies. The block diagram of the proposed control approach with the EPS modulation is depicted in Fig. 7. The proposed method is implemented by using the TMS320F28379D MCU from Texas Instruments. Voltages are measured via LV-25 voltage sensors. The system parameters used in the experimental and simulation studies are listed in Table 1. The control parameters are considered as  $\varepsilon = 0.4$ ,  $l_o = 0.01$ ,  $l_1 = 0.1$ ,  $\lambda = 10$ , and  $\beta = 100$ .

TABLE 1. System parameters.

Description and Symbol	Value
Input voltage ( $V_{in}$ )	30-70 V
Output voltage ( $V_o$ )	50 and 60 V
Transformer turn ratio (N)	N=1
Equivalent series inductor referred to the primary ( $L$ )	0.02mH
related resistance of the inductor ( $R$ )	0.001Ω
Sampling/switching frequency	40kHz
Output capacitor ( $C$ )	200 μF
Load resistance ( $R_L$ )	20-40 Ω

Fig.8 shows the comprehensive flowchart of the proposed ONO algorithm, along with the ASTSMC. First, the reference output voltage ( $V_o^*$ ) is defined, and then the required variables ( $V_o$ ,  $V_{in}$ ) are measured using sensors. The control method is then launched by calculating the sliding manifold ( $\sigma$ ),  $k_1$  and  $k_2$  by using equations (25), (31.a), and (32). Next, the control law equation in (29) is used to generate the control signal ( $\delta_o$ ). The optimization rule is initiated by calculating the voltage conversion ratio ( $k$ ), and the resulting block yields the optimal value of  $\delta_{in}$ . Finally, both  $\delta_o$  and  $\delta_{in}$  are transferred to the modulation block to complete the cycle. Both  $\delta_o$  and  $\delta_{in}$  are updated through the algorithm in the presence of abrupt changes in the operating point of the DAB.

### A. STEADY-STATE AND TRANSIENT RESPONSE RESULTS

The experimental results in steady-state obtained by the proposed ONO ASTSMC method under boost and buck modes are shown in Fig. 9(a) and (b) and (c), respectively.



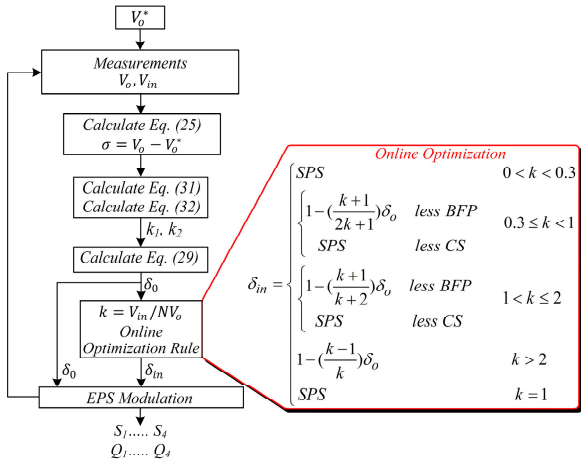


FIGURE 8. Flowchart for the proposed optimization plus ASTSMC algorithm.

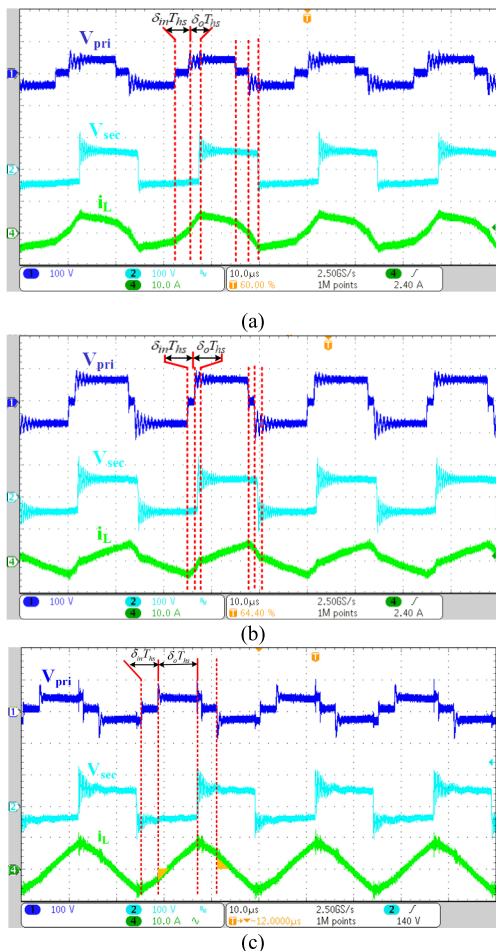


FIGURE 9. Steady state responses. (a) Boost operation with  $V_{in} = 40V$ ,  $V_o = 50V$  with ONO ASTSMC method, (b) Buck operation with  $V_{in} = 70V$ ,  $V_o = 50V$  with ONO ASTSMC method, (c) Boost operation with  $V_{in} = 40V$ ,  $V_o = 50V$  without optimization method.

Fig. 9(a) shows  $V_{pri}$ ,  $V_{sec}$ , and  $i_L$  under boost operation when  $V_{in}=40V$  and  $V_o=50V$ . To verify if ONO is capable

of optimizing the internal phase shift and improving the efficiency, the BFP is taken into account. To elaborate the BFP minimization, both inductor current and primary voltage ( $V_{pri}$ ) are considered in one switching cycle. Apparently, both  $V_{pri}$  and  $i_L$  polarities are same in the whole switching cycle which states that the BFP is zero. When BFP is zero, the inductor current stress also attains to its minimum value according to Fig.9(a). Similarly, both BFP and CS are optimized in the buck mode when  $V_{in}=70V$  and  $V_o=50V$  which is shown in Fig. 9(b). To verify the performance of the ONO method, the same system is analyzed without any optimization method in Fig. 9(c), and the results are compared to those obtained using the proposed control method. This comparison is made to determine how the CS and BFP are optimized under the proposed method. To achieve the same operating point as Fig.9 (a),  $\delta_{in}$  and  $\delta_o$  are regulated manually under boost operation while  $V_{in}=40V$  and  $V_o=50V$ . In Fig. 9(c), the BFP is illustrated as highlighted dark yellow in the inductor current and if it is compared with Fig. 9(a), which has approximately zero BFP, the effectiveness of the proposed method in decreasing the BFP losses can be seen. To compare the CS reduction capability of the proposed method, the inductor current stress in both figures can be compared. Obviously, the CS of the inductor current in Fig. 9(c) is more than that of the proposed method. Therefore, it can be concluded that, under the same operating point, the proposed online optimization method regulates  $\delta_{in}$  in such a way that it decreases both BFP and CS simultaneously.

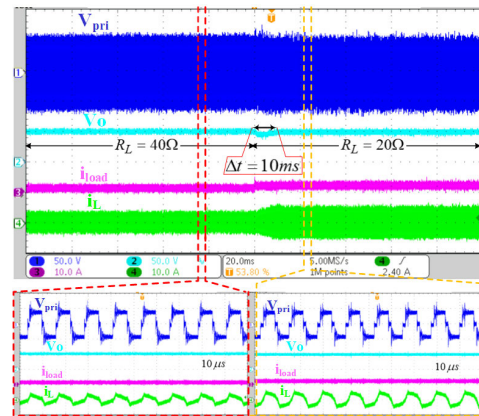


FIGURE 10. Transient responses of the ASTSMC under load variation.

In the next step, the transient response of the system under different disturbances including load change, output voltage reference variation and input voltage variation is elaborated. The results are shown in Figs.10 -12.

The transient behavior of the proposed method for an abrupt change in  $R_L$  from  $40\Omega$  to  $20\Omega$  is shown in Fig. 10. This test is performed under boost mode while  $V_{in} = 40V$ , and  $V_o^* = 50V$ . The load change is applied to the system and the behavior of the variables are observed. Taking into account the variations of  $V_o$ , one can see that  $V_o$  is regulated at  $50V$  after  $i_{load}$  is changed. Although a

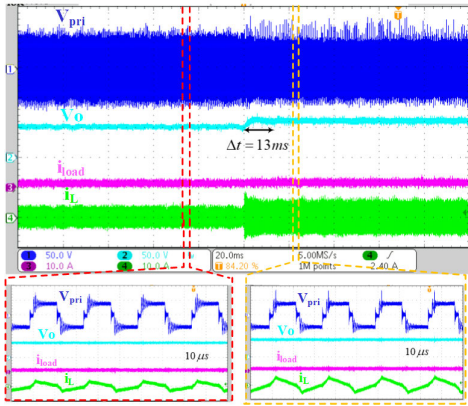


FIGURE 11. Transient responses of the ASTSMC under variations in  $V_o^*$ .

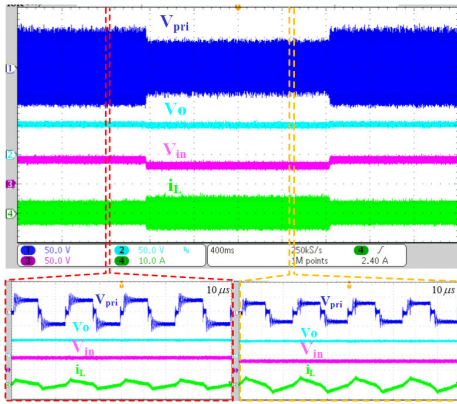


FIGURE 12. Transient responses of the ASTSMC under input voltage variation.

small undershoot occurs in  $V_o$ , it is corrected within 10ms. Obviously,  $i_L$  and  $i_{load}$  are increased after the load change.

Fig. 11 depicts the transient responses of the proposed method to a sudden increase in  $V_o^*$  from 50V to 60V. As shown in the plot,  $V_o$  tracks the reference voltage (60V) after a settling time of 13ms. It is worth noting that the amplitude of  $V_{pri}$  remains unchanged since  $V_{in}$  is constant. However, due to the increase in  $V_o$ , the output power slightly increases leading to an increase in the inductor current ( $i_L$ ).

Fig. 12 illustrates the transient response of the proposed method to a step change in the input voltage ( $V_{in}$ ) from 40V to 30V and then restored back to 40V again. Clearly,  $V_{pri}$  is reduced depending on the change in  $V_{in}$  as stated in (15). Since  $V_{in}$  is reduced when the output power is constant,  $i_L$  is also increased. Also,  $V_o$  tracks  $V_o^*$  without suffering from the disturbance. To further evaluate the BFP optimization of the method, the polarity of the  $V_{pri}$  and  $i_L$  can be tested in one switching time before and after the disturbance. Obviously, the BFP is approximately zero, since  $\delta_{in}$  is tuned in such a way to derive zero  $V_{pri}$  while the polarity of the inductor is opposite.

To quantitatively evaluate the transient performance of the proposed method and compare it with a conventional

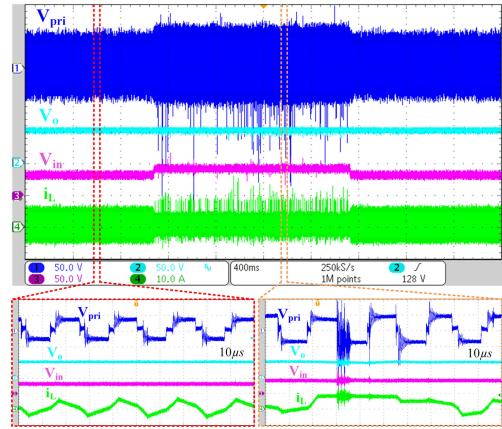


FIGURE 13. Transient responses of conventional STSMC under variations in  $V_{in}$ .

STSMC approach, the same step change in the input voltage from 40V to 30V and then back to 40V is applied to the system under conventional STSMC in Fig.13 and Fig.13 is compared to Fig.12. The test is conducted using the same circuit and load conditions for both methods, and the control

parameters of the conventional STSMC are derived according to [39] and overestimated to keep the system stable. Nevertheless, while  $V_{in}$  is increased to 40V, the control method fails to suppress chattering and needs the variation of the coefficient manually to improve the chattering reduction. On the other hand, while the system returns back to the steady state, the conventional STSMC continues working with the overestimated maximum coefficient while the proposed ASTSMC switches back to the minimum coefficient.

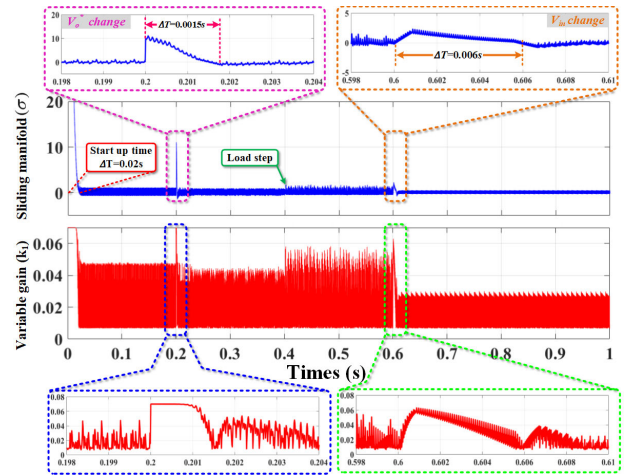


FIGURE 14. Sliding manifold and the variable gain under ASTSMC.

In order to demonstrate the superiority of the ASTSMC over the conventional STSMC analyzing the sliding surface and the control law gains, both methods are applied to the DAB converter and their performance are compared. Specifically, simulations using the same circuit and load conditions for both methods are conducted. The results are depicted in Fig. 14 and Fig. 15. Fig. 14 shows the simulation results of  $\sigma$  and  $k_1$  under perturbations of  $R_L$ ,  $V_{in}$ , and  $V_o^*$ .

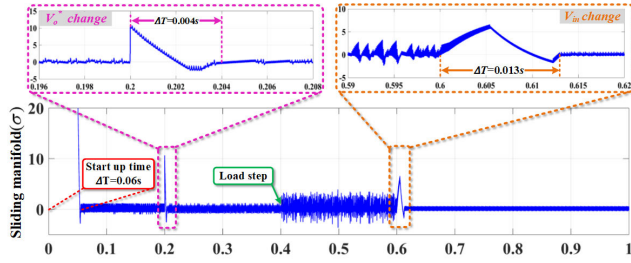


FIGURE 15. Sliding manifold under conventional STSMC.

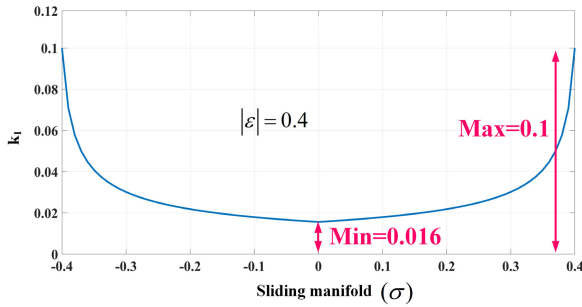
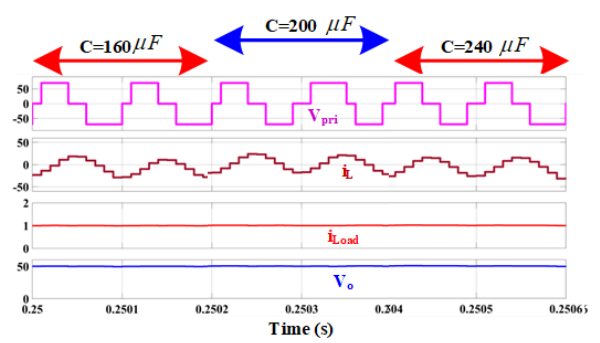
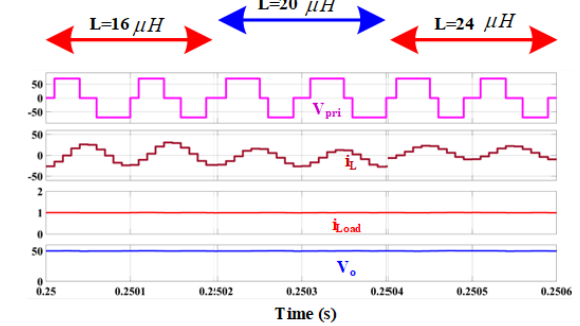


FIGURE 16. Variation of  $k_1$  against  $\sigma$  for  $|\sigma| < \epsilon$ .

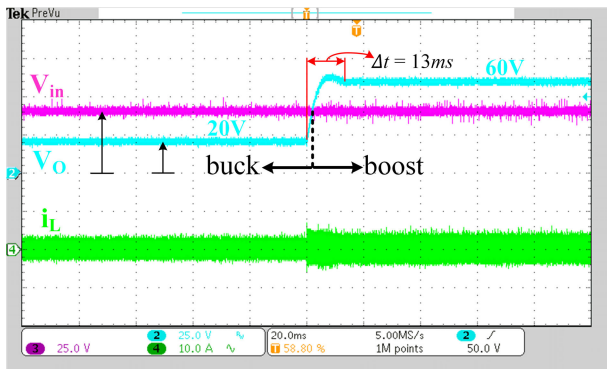


(a)

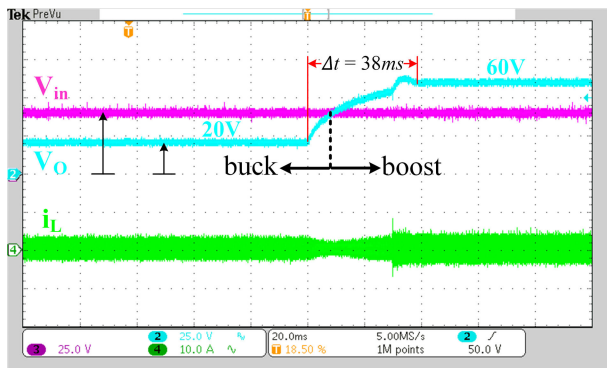


(b)

FIGURE 18. The performance of the proposed control method under: (a)  $\pm 20\%$  variation in the capacitor value, (b)  $\pm 20\%$  variation in the inductor value.



(a)



(b)

FIGURE 17. The effect of variation of  $\lambda$  on the dynamic response of output voltage under output voltage reference change. (a)  $\lambda = 10$ , (b)  $\lambda = 1$ .

As one can see at  $t = 0.2s$ , a disturbance (step change in  $V_o^*$ ) is applied to the system. Obviously, the gain is increased exponentially until the sliding motion

reaches  $\sigma$  and after a short time (0.0015s) the system returns back to the steady state. In order to observe the behavior of  $\sigma$  and  $k_1$ ,  $V_{in}$  is changed at  $t=0.6s$ . As a result of this change,  $k_1$  increases and returns back to its normal value after 0.006s. Fig. 15 shows the sliding surface obtained by the constant gain based STSMC under same disturbances. It is worth mentioning that an overestimated constant gain ( $k_1$ ) is considered for the conventional STSMC to get a good performance. Comparing Fig. 14 and Fig. 15, demonstrate the excellent performance of the proposed method. Clearly the response of  $k_1$  is faster than that of the constant gain since  $k_1$  tunes itself according to the variations of the sliding function. Also, the constant gain method requires an overestimated gain for both steady-state and transient operation of the DAB converter while the proposed ASTSMC can tune  $k_1$  under different situations based on the magnitude of the error. Therefore, the proposed method successfully tracks the reference voltage, while minimizing the overshoot and settling time. Moreover, the proposed method shows better robustness compared to the conventional STSMC, as it can handle the perturbations and maintain the steady-state output voltage and current.

### B. REMARKS ON THE PARAMETER SELECTION

The proposed ASTSMC method is designed based on adaptive variation of the key control parameters ( $k_1$  and  $k_2$ ), as outlined in (31.a) and (31.b). These parameters are carefully



TABLE 2. Comparison of the proposed method with the existing methods in literature.

Items	[5]	[6]	[11]	[12]	[23]	[24]	[26]	[41]	[42]	Proposed method
Topology	DAB	DAB	DAB	DAB	Modular DAB	DAB	DAB	Current fed (CFDAB)	DAB	DAB
Optimization goal	BFP, CS	BFP	CS	BFP, CS	CS	Not optimization	Not optimization	ZVS	Not optimization	BFP, CS
Modulation method	EPS	EPS	UPS	EPS, DPS	DPS	SPS	SPS	Decoupled dual PWM	SPS	EPS
Number of sensors	Not clear	3 sensors ( $V_o, V_{in}, i_o$ )	2 sensors ( $V_o, V_{in}$ )	3 sensors ( $V_o, V_{in}, i_o$ )	3 sensors ( $V_o, V_{in}, i_{in}$ )	2 sensors ( $V_o, V_{in}$ )	4 sensors ( $V_o, V_{in}, i_o, i_{in}$ )	3 sensors ( $V_o, V_{in}, i_{in}$ )	4 sensors ( $V_o, V_{in}, i_o, i_{dc}$ )	2 sensors ( $V_o, V_{in}$ )
Control method	Open loop	Closed loop (PI controller)	Closed loop (PI controller)	Closed loop (PI controller)	Closed loop (PI &MPC)	Closed loop (PI &MPC)	Closed loop (SMC)	Closed loop (PI & MPC)	Closed loop (MPC)	Closed loop (ASTSMC)
Optimization method	Tracking the power curve (OFFO)	Using Karush–Kuhn–Tucker function (OFFO)	LMM ONO	OFFO (using look up table) Parameter based method	LMM OFFO	N.A.	N.A.	Natural commutation strategy	N.A.	LMM ONO
Time Duration (TD)of dynamic response to load change	N.A.	No result reported	No result reported	No result reported	Fast (TD not reported)	Fast (TD not reported)	25ms delay	300ms delay	15ms delay	10ms delay
Sensitivity to parameters	N.A.	No result reported	No result reported	No result reported	High	Moderate	Low	High	High	Low

tuned to ensure that the method achieves fast and accurate tracking of the reference voltage, while minimizing the overshoot and settling time. When  $\sigma$  deviates from the predefined value, which is null (0), variations in  $k_1$  force  $\sigma$  to move zero again. Since the removal of chattering and attaining an exactly zero chattering is impossible in real applications, a very small positive error ( $\varepsilon$ ) can be considered as mentioned in [33]. When the magnitude of  $\sigma$  is less than the predefined error, then ((31.a)) determines  $k_1$ . Equation ((31.a)) is a barrier function which starts functioning while  $\sigma$  is confined in the error barrier ( $|\varepsilon| = 0.4$ ) as shown in Fig. 16. Clearly, when  $\sigma$  is approximately null,  $k_1$  decreases to its least value which is a positive number ( $k_1(0) = \frac{I_o}{\sqrt{\varepsilon}}$ ). It is a saturation point to keep the control input between 0 and 1.

The performance of the proposed ASTSMC method is primarily determined by the choice of  $\lambda$  given in (31.b).  $\lambda$  directly affects the control response of the DAB converter, with higher values leading to faster system dynamics. To investigate the impact of  $\lambda$  on dynamic response of the system, the output voltage reference is increased from 20V to 60V which is shown in Fig. 17. The system is tested under reference voltage variation for two different values of  $\lambda$ . When  $\lambda = 10$ , the load voltage tracks the set point (60V) in 13ms. On the other hand, when  $\lambda = 1$ , the load voltage reaches to the set point (60 V) in 38ms. Therefore, increasing  $\lambda$  leads to rapid growth of  $k_1$  and consequently improves the dynamic response.

C. ROBUSTNESS TEST AGAINST PARAMETER VARIATIONS

To investigate the robustness of the proposed control strategy, the simulations are carried out by varying the values of capacitors and inductors in the DAB converter by  $\pm 20\%$ . The goal was to assess the performance of proposed controller under parameter variations. The simulation results given in Fig. 18 show that the proposed control strategy is indeed robust to parameter variations. Specifically, the load voltage was able to track the reference voltage with high accuracy and minimal deviation, even when the values of the capacitors and inductors were varied by  $\pm 20\%$ .

D. COMPARISON WITH EXISTING METHODS

Table 2 gives a brief comparison between the proposed control method and state of the art. All the methods are compared regarding various items such as the modulation strategy, the optimization goal, the number of sensors, the control method, the optimization method, and dynamic response. Obviously, one can see that the proposed method achieves the optimization of BFP and CS simultaneously by using two sensors only. On the other hand, the proposed method employs an ONO method which takes its strength from a robust ASTSMC scheme that is responsible for generating the outer phase shift ratio. Among the control methods shown in Table 2, the proposed control method has the fastest dynamic response.



**TABLE 3.** Comparison of the proposed method with the existing online methods.

Items	[11]	[17]	[18]	[19]	Proposed method
Topology	DAB	Half bridge DAB	DAB	DAB	DAB
Optimization goal	CS	Input current (CS)	CS-ZVS	CS	BFP, CS
Modulation method	UPS	-	Hybrid TPS	AI-based TPS	EPS
Output voltage Control method	PI	PI	PID	PI	ASTSMC
Optimization method	LMM	simplex-based optimizer (SMO)	Using analytical Piecewise Model	Neural network and fuzzy inference system	LMM
Simplicity	Medium	Complicated	Complicated	Complicated	Simple

In order to highlight the benefits of ONO method proposed in this study, we compared it with other existing online methods and compiled the results in Table 3. The purpose of this comparison is to demonstrate the superior performance of ONO method in terms of accuracy, efficiency, and reliability, and to identify its potential advantages for practical applications.

This table (Table 3) presents an overview of the key features including the topology, optimization goal, modulation method, output voltage control method optimization method and degree of simplicity. Our analysis shows that ONO method outperforms the other methods in terms of accuracy of the closed loop control and computational simplicity, while also exhibiting high reliability and robustness under a variety of conditions due to the application of ASTSMC.

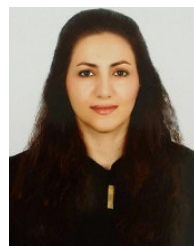
## VI. CONCLUSION

This paper proposes an approach that utilizes adaptive super-twisting sliding mode control (ASTSMC) and online optimization to improve the performance of a dual active bridge (DAB) converter under extended phase shift modulation. The ASTSMC generates the outer phase shift ratio, while an optimization rule is used to minimize the inductor current stress (CS) and backflow power (BFP) and generate the inner phase shift ratio. The presented strategy not only enhances the converter's efficiency, but also considers the error around the sliding manifold when tuning the outer phase shift ratio. Simulation and experimental results demonstrate that the proposed strategy effectively decreases both BFP and CS under EPS modulation and improves the time response. The paper also investigates the dynamic behavior of the proposed control method. Comparative results obtained under constant and variable gain STSMC methods highlight the proposed method's ability to avoid overestimating gains while decreasing the time response effectively.

## REFERENCES

- [1] M. H. Kheraluwala, R. W. Gasgoigne, D. M. Divan, and E. Bauman, "Performance characterization of a high power dual active bridge DC/DC converter," in *Proc. Conf. Rec. IEEE Ind. Appl. Soc. Annu. Meeting*, Seattle, WA, USA, Nov. 1998, pp. 3920–3924.
- [2] N. Hou and Y. W. Li, "Overview and comparison of modulation and control strategies for a nonresonant single-phase dual-active-bridge DC–DC converter," *IEEE Trans. Power Electron.*, vol. 35, no. 3, pp. 3148–3172, Mar. 2020, doi: [10.1109/TPEL.2019.2927930](https://doi.org/10.1109/TPEL.2019.2927930).
- [3] S. Shao, H. Chen, X. Wu, J. Zhang, and K. Sheng, "Circulating current and ZVS-on of a dual active bridge DC–DC converter: A review," *IEEE Access*, vol. 7, pp. 50561–50572, 2019, doi: [10.1109/ACCESS.2019.2911009](https://doi.org/10.1109/ACCESS.2019.2911009).
- [4] R. W. A. A. De Doncker, D. M. Divan, and M. H. Kheraluwala, "A three-phase soft-switched high-power-density DC/DC converter for high-power applications," *IEEE Trans. Ind. Appl.*, vol. 27, no. 1, pp. 63–73, Jan./Feb. 1991.
- [5] B. Zhao, Q. Yu, and W. Sun, "Extended-phase-shift control of isolated bidirectional DC–DC converter for power distribution in microgrid," *IEEE Trans. Power Electron.*, vol. 27, no. 11, pp. 4667–4680, Nov. 2012, doi: [10.1109/TPEL.2011.2180928](https://doi.org/10.1109/TPEL.2011.2180928).
- [6] H. Shi, H. Wen, J. Chen, Y. Hu, L. Jiang, G. Chen, and J. Ma, "Minimum-backflow-power scheme of DAB-based solid-state transformer with extended-phase-shift control," *IEEE Trans. Ind. Appl.*, vol. 54, no. 4, pp. 3483–3496, Jul. 2018, doi: [10.1109/TIA.2018.2819120](https://doi.org/10.1109/TIA.2018.2819120).
- [7] F. An, W. Song, K. Yang, S. Luo, and X. Feng, "Optimised power control and balance scheme for the output parallel dual-active-bridge DC–DC converters in power electronic traction transformer," *IET Power Electron.*, vol. 12, no. 9, pp. 2295–2303, Aug. 2019, doi: [10.1049/iet-pel.2018.5056](https://doi.org/10.1049/iet-pel.2018.5056).
- [8] B. Zhao, Q. Song, W. Liu, and W. Sun, "Current-stress-optimized switching strategy of isolated bidirectional DC–DC converter with dual-phase-shift control," *IEEE Trans. Ind. Electron.*, vol. 60, no. 10, pp. 4458–4467, Oct. 2013, doi: [10.1109/TIE.2012.2210374](https://doi.org/10.1109/TIE.2012.2210374).
- [9] B. Zhao, Q. Song, and W. Liu, "Efficiency characterization and optimization of isolated bidirectional DC–DC converter based on dual-phase-shift control for DC distribution application," *IEEE Trans. Power Electron.*, vol. 28, no. 4, pp. 1711–1727, Apr. 2013, doi: [10.1109/TPEL.2012.2210563](https://doi.org/10.1109/TPEL.2012.2210563).
- [10] H. Wen and B. Su, "Reactive power and soft-switching capability analysis of dual-active-bridge DC–DC converters with dual-phase-shift control," *J. Power Electron.*, vol. 15, no. 1, pp. 18–30, Jan. 2015, doi: [10.6113/JPE.2015.15.1.18](https://doi.org/10.6113/JPE.2015.15.1.18).
- [11] N. Hou, W. Song, and M. Wu, "Minimum-current-stress scheme of dual active bridge DC–DC converter with unified phase-shift control," *IEEE Trans. Power Electron.*, vol. 31, no. 12, pp. 8552–8561, Dec. 2016, doi: [10.1109/TPEL.2016.2521410](https://doi.org/10.1109/TPEL.2016.2521410).
- [12] N. Noroozi, A. Emadi, and M. Narimani, "Performance evaluation of modulation techniques in single-phase dual active bridge converters," *IEEE Open J. Ind. Electron. Soc.*, vol. 2, pp. 410–427, 2021, doi: [10.1109/OJIES.2021.3087418](https://doi.org/10.1109/OJIES.2021.3087418).
- [13] L. Chen, L. Lin, S. Shao, F. Gao, Z. Wang, P. W. Wheeler, and T. Dragicevic, "Moving discretized control set model-predictive control for dual-active bridge with the triple-phase shift," *IEEE Trans. Power Electron.*, vol. 35, no. 8, pp. 8624–8637, Aug. 2020, doi: [10.1109/TPEL.2019.2962838](https://doi.org/10.1109/TPEL.2019.2962838).
- [14] S. Shao, M. Jiang, W. Ye, Y. Li, J. Zhang, and K. Sheng, "Optimal phase-shift control to minimize reactive power for a dual active bridge DC–DC converter," *IEEE Trans. Power Electron.*, vol. 34, no. 10, pp. 10193–10205, Oct. 2019, doi: [10.1109/TPEL.2018.2890292](https://doi.org/10.1109/TPEL.2018.2890292).

- [15] F. Xu, J. Liu, and Z. Dong, "Minimum backflow power and ZVS design for dual-active-bridge DC–DC converters," *IEEE Trans. Ind. Electron.*, vol. 70, no. 1, pp. 474–484, Jan. 2023, doi: [10.1109/TIE.2022.3156159](https://doi.org/10.1109/TIE.2022.3156159).
- [16] D. Das and K. Basu, "Optimal design of a dual-active-bridge DC–DC converter," *IEEE Trans. Ind. Electron.*, vol. 68, no. 12, pp. 12034–12045, Dec. 2021, doi: [10.1109/TIE.2020.3044781](https://doi.org/10.1109/TIE.2020.3044781).
- [17] F. Bez, L. Scandola, L. Corradini, S. Saggini, and G. Spiazzi, "Two-dimensional online efficiency optimization technique for dual active bridge converters," in *Proc. IEEE 17th Workshop Control Model. Power Electron. (COMPEL)*, Trondheim, Norway, Jun. 2016, pp. 1–8, doi: [10.1109/COMPEL.2016.7556669](https://doi.org/10.1109/COMPEL.2016.7556669).
- [18] A. K. Bhattacharjee and I. Batarseh, "Optimum hybrid modulation for improvement of efficiency over wide operating range for triple-phase-shift dual-active-bridge converter," *IEEE Trans. Power Electron.*, vol. 35, no. 5, pp. 4804–4818, May 2020, doi: [10.1109/TPEL.2019.2943392](https://doi.org/10.1109/TPEL.2019.2943392).
- [19] X. Li, X. Zhang, F. Lin, C. Sun, and K. Mao, "Artificial-intelligence-based triple phase shift modulation for dual active bridge converter with minimized current stress," *IEEE J. Emerg. Sel. Topics Power Electron.*, vol. 11, no. 4, pp. 4430–4441, Aug. 2023, doi: [10.1109/JESTPE.2021.3105522](https://doi.org/10.1109/JESTPE.2021.3105522).
- [20] X. Meng, Y. Jia, Q. Xu, C. Ren, X. Han, and P. Wang, "A novel intelligent nonlinear controller for dual active bridge converter with constant power loads," *IEEE Trans. Ind. Electron.*, vol. 70, no. 3, pp. 2887–2896, Mar. 2023, doi: [10.1109/TIE.2022.3170608](https://doi.org/10.1109/TIE.2022.3170608).
- [21] L. Deng, G. Zhou, Q. Bi, and N. Xu, "Online reactive power minimization and soft switching algorithm for triple-phase-shift modulated dual active bridge converter," *IEEE Trans. Ind. Electron.*, vol. 70, no. 3, pp. 2543–2555, Mar. 2023, doi: [10.1109/TIE.2022.3169713](https://doi.org/10.1109/TIE.2022.3169713).
- [22] C. Song, A. Sangwongwanich, Y. Yang, and F. Blaabjerg, "A model-free capacitor voltage balancing method for multilevel DAB converters," *IEEE Trans. Power Electron.*, vol. 38, no. 1, pp. 79–84, Jan. 2023, doi: [10.1109/TPEL.2022.3203746](https://doi.org/10.1109/TPEL.2022.3203746).
- [23] S. Shao, L. Chen, Z. Shan, F. Gao, H. Chen, D. Sha, and T. Dragicevic, "Modeling and advanced control of dual-active-bridge DC–DC converters: A review," *IEEE Trans. Power Electron.*, vol. 37, no. 2, pp. 1524–1547, Feb. 2022, doi: [10.1109/TPEL.2021.3108157](https://doi.org/10.1109/TPEL.2021.3108157).
- [24] F. An, W. Song, B. Yu, and K. Yang, "Model predictive control with power self-balancing of the output parallel DAB DC–DC converters in power electronic traction transformer," *IEEE J. Emerg. Sel. Topics Power Electron.*, vol. 6, no. 4, pp. 1806–1818, Dec. 2018, doi: [10.1109/JESTPE.2018.2823364](https://doi.org/10.1109/JESTPE.2018.2823364).
- [25] F. An, W. Song, K. Yang, N. Hou, and J. Ma, "Improved dynamic performance of dual active bridge DC–DC converters using MPC scheme," *IET Power Electron.*, vol. 11, no. 11, pp. 1756–1765, Sep. 2018, doi: [10.1049/iet-pel.2017.0707](https://doi.org/10.1049/iet-pel.2017.0707).
- [26] T. Samad, M. Bauer, S. Bortoff, S. Di Cairano, L. Fagiano, P. F. Odgaard, R. R. Rhinehart, R. Sánchez-Peña, A. Serbezov, F. Ankersen, P. Goupil, B. Grosman, M. Heertjes, I. Mareels, and R. Sossch, "Industry engagement with control research: Perspective and messages," *Annu. Rev. Control*, vol. 49, pp. 1–14, Jan. 2020.
- [27] Y.-C. Jeung and D.-C. Lee, "Voltage and current regulations of bidirectional isolated dual-active-bridge DC–DC converters based on a double-integral sliding mode control," *IEEE Trans. Power Electron.*, vol. 34, no. 7, pp. 6937–6946, Jul. 2019, doi: [10.1109/TPEL.2018.2873834](https://doi.org/10.1109/TPEL.2018.2873834).
- [28] S. Lee, Y.-C. Jeung, and D.-C. Lee, "Voltage balancing control of IPOS modular dual active bridge DC/DC converters based on hierarchical sliding mode control," *IEEE Access*, vol. 7, pp. 9989–9997, 2019, doi: [10.1109/ACCESS.2018.2889345](https://doi.org/10.1109/ACCESS.2018.2889345).
- [29] N. Tiwary, A. K. Panda, R. K. Lenka, and A. Narendra, "Super twisting sliding mode control of dual active bridge DC–DC converter," in *Proc. IEEE Int. Conf. Power Electron., Drives Energy Syst. (PEDES)*, Dec. 2020, pp. 1–5, doi: [10.1109/PEDES49360.2020.9379589](https://doi.org/10.1109/PEDES49360.2020.9379589).
- [30] F. Bagheri, N. Guler, and H. Komurcugil, "Sliding mode current observer for a bidirectional dual active bridge converter," in *Proc. 47th Annu. Conf. IEEE Ind. Electron. Soc.*, Oct. 2021, pp. 1–6, doi: [10.1109/IECON48115.2021.9589703](https://doi.org/10.1109/IECON48115.2021.9589703).
- [31] E. Abdelkarim and S. Kadi, "Super twisted sliding mode control of isolated bidirectional DC–DC converter in electric vehicle," in *Proc. 22nd Int. Middle East Power Syst. Conf. (MEPCON)*, Dec. 2021, pp. 389–394, doi: [10.1109/MEPCON50283.2021.9686192](https://doi.org/10.1109/MEPCON50283.2021.9686192).
- [32] N. Tiwary, V. R. N. Naik, A. K. Panda, R. K. Lenka, and A. Narendra, "Sliding mode and current observer-based direct power control of dual active bridge converter with constant power load," *Int. Trans. Elect. Energy Syst.*, vol. 31, no. 5, 2021, Art. no. e12879.
- [33] T. Gonzalez, J. A. Moreno, and L. Fridman, "Variable gain super-twisting sliding mode control," *IEEE Trans. Autom. Control*, vol. 57, no. 8, pp. 2100–2105, Aug. 2012.
- [34] Y. Shtessel, M. Taleb, and F. Plestan, "A novel adaptive-gain supertwisting sliding mode controller: Methodology and application," *Automatica*, vol. 48, no. 5, pp. 759–769, May 2012, doi: [10.1016/j.automatica.2012.02.024](https://doi.org/10.1016/j.automatica.2012.02.024).
- [35] H. Obeid, S. Laghrouche, L. Fridman, Y. Chitour, and M. Harmouche, "Barrier function-based adaptive super-twisting controller," *IEEE Trans. Autom. Control*, vol. 65, no. 11, pp. 4928–4933, Nov. 2020, doi: [10.1109/TAC.2020.2974390](https://doi.org/10.1109/TAC.2020.2974390).
- [36] F. S. Hillier, *Introduction To Operations Research: Concepts and Cases*, 8th ed. New York, NY, USA: McGraw-Hill, Jan. 2007.
- [37] H. Qin and J. W. Kimball, "Generalized average modeling of dual active bridge DC–DC converter," *IEEE Trans. Power Electron.*, vol. 27, no. 4, pp. 2078–2084, Apr. 2012.
- [38] D. Segaran, D. G. Holmes, and B. P. McGrath, "Enhanced load step response for a bidirectional DC–DC converter," *IEEE Trans. Power Electron.*, vol. 28, no. 1, pp. 371–379, Jan. 2013, doi: [10.1109/TPEL.2012.2200505](https://doi.org/10.1109/TPEL.2012.2200505).
- [39] J. A. Moreno and M. Osorio, "Strict Lyapunov functions for the super-twisting algorithm," *IEEE Trans. Autom. Control*, vol. 57, no. 4, pp. 1035–1040, Apr. 2012, doi: [10.1109/TAC.2012.2186179](https://doi.org/10.1109/TAC.2012.2186179).
- [40] A. Chalanga, S. Kamal, L. M. Fridman, B. Bandyopadhyay, and J. A. Moreno, "Implementation of super-twisting control: Super-twisting and higher order sliding-mode observer-based approaches," *IEEE Trans. Ind. Electron.*, vol. 63, no. 6, pp. 3677–3685, Jun. 2016, doi: [10.1109/TIE.2016.2523913](https://doi.org/10.1109/TIE.2016.2523913).
- [41] R. Seeber, M. Reichhartinger, and M. Horn, "A Lyapunov function for an extended super-twisting algorithm," *IEEE Trans. Autom. Control*, vol. 63, no. 10, pp. 3426–3433, Oct. 2018, doi: [10.1109/TAC.2018.2794411](https://doi.org/10.1109/TAC.2018.2794411).
- [42] Y. Zhang, Z. Wang, Y. W. Li, N. Hou, and M. Cheng, "Decoupled dual-PWM control for naturally commutated current-fed dual-active-bridge DC/DC converter," *IEEE J. Emerg. Sel. Topics Power Electron.*, vol. 8, no. 4, pp. 4246–4259, Dec. 2020, doi: [10.1109/JESTPE.2019.2933316](https://doi.org/10.1109/JESTPE.2019.2933316).
- [43] L. Chen, S. Shao, Q. Xiao, L. Tarisciotti, P. W. Wheeler, and T. Dragicevic, "Model predictive control for dual-active-bridge converters supplying pulsed power loads in naval DC micro-grids," *IEEE Trans. Power Electron.*, vol. 35, no. 2, pp. 1957–1966, Feb. 2020, doi: [10.1109/TPEL.2019.2917450](https://doi.org/10.1109/TPEL.2019.2917450).



**FARZANEH BAGHERI** (Member, IEEE) received the B.Sc. degree in power electrical engineering from Shahid Beheshti University, Tehran, Iran, in 2005, the M.Sc. degree in power electrical engineering from Azarbaijan Shahid Madani University, Tabriz, Iran, in 2010, and the Ph.D. degree (Hons.) in electrical engineering from Eastern Mediterranean University (EMU), Famagusta, North Cyprus, Turkey, in 2019. She is currently an Assistant Professor with the Electrical and Electronics Engineering Department, Antalya Bilim University, Antalya, Turkey. Her research interests include power electronics, nonlinear control methods for power electronic converters, and sliding mode control.



**NAKI GULER** (Senior Member, IEEE) received the B.Sc., M.Sc., and Ph.D. degrees in electrical and electronic engineering from Gazi University, Ankara, Turkey, in 2010, 2012, and 2019, respectively. He joined the Department of Electricity and Energy, Gazi University, in 2012. His current research interests include control and applications of power electronic converters, energy conversion, and energy management of renewable sources. He was a recipient of IEEE IES Young Professionals Student Paper Travel Award at 12th CPE-POWERENG, in 2018, and best paper awards at the Sixth ICRERA and 12th CPE-POWERENG Conferences.



**HASAN KOMURCUGIL** (Senior Member, IEEE) received the B.Sc., M.Sc., and Ph.D. degrees in electrical engineering from Eastern Mediterranean University (EMU), Famagusta, North Cyprus, Turkey, in 1989, 1991, and 1998, respectively. He is currently a full-time Professor with the Computer Engineering Department, EMU. He serves as an Associate Editor for the IEEE TRANSACTIONS ON INDUSTRIAL ELECTRONICS and the IEEE TRANSACTIONS ON INDUSTRIAL INFORMATICS.



**SERTAC BAYHAN** (Senior Member, IEEE) received the M.S. and Ph.D. degrees in electrical engineering from Gazi University, Ankara, Turkey, in 2008 and 2012, respectively. He has acquired 13 MUSD in research funding and published more than 170 papers in mostly prestigious IEEE journals and conferences. He is the coauthor of three books and six book chapters. He was a recipient of many prestigious international awards, such as the Research Fellow Excellence Award in recognition of his research achievements and exceptional contributions to Texas A&M University at Qatar, in 2018; the Best Paper Presentation Recognition at the 41st and 42nd Annual Conference of the IEEE Industrial Electronics Society, in 2015 and 2016; the Research Excellence Travel Awards (Texas A&M University at Qatar), in 2014 and 2015; and the Researcher Support Awards from the Scientific and Technological Research Council of Turkey (TUBITAK). He currently serves as an Associate Editor for IEEE TRANSACTIONS ON INDUSTRIAL ELECTRONICS, IEEE JOURNAL OF EMERGING AND SELECTED TOPICS IN INDUSTRIAL ELECTRONICS, IEEE OPEN JOURNAL OF THE INDUSTRIAL ELECTRONICS SOCIETY, and IEEE Industrial Electronics Technology News.

...